Scattering, inelastic: Electron

Dimitri D. Vvedensky[a], and Mehmet Erbudak[b], [a] The Blackett Laboratory, Imperial College London, London, United Kingdom and [b] Solid State Physics, ETHZ, Zürich, Switzerland

Abstract

An interaction event between an electron and a target material is called inelastic if the electron loses some or all of its energy. The general theory of the inelastic scattering cross-section is first developed before being specialized to interband transitions, plasmon excitations, vibrations at surfaces, core-electron excitations, and (e^-, $2e^-$) scattering. Examples are provided to illustrate how the elementary excitations of each method provide information about the atomic structure and electronic properties of materials, often in conjunction with density-functional calculations.

- Differential cross-section for inelastically scattered electrons, including dielectric formulation for interband transitions.
- Extensions to plasma excitations, vibrations at surfaces, excitations of core electrons, and (e^-, $2e^-$) scattering.
- Example of each application of inelastic electron scattering.
- Discussion of theoretical and computational approaches to inelastic scattering, including symmetry analysis, identification of paths in multiple scattering, and density functional methods.

Keywords(e^-, $2e^-$) ScatteringCore excitationsDensity functional methodsExtended fine structureInelastic electron ScatteringInterband transitionsKramers–KronigNear-edge fine structurePlasmonsScattering cross-sectionSelection rulesSurface vibrations

Introduction

Inelastic electron scattering phenomena are used to obtain information on the electronic properties and atomic structure of materials. An interaction event between an electron and a target material is called inelastic if the electron loses some or all of its energy. Otherwise, the event is called elastic. Any energy loss by the electron is equal to the energy gained by the material and is characteristic of the type of scattering event. The measurement of an inelastic event determines the energy transferred and the rate of this transfer, which provides physical information about the elementary excitations of the material.

Inelastic interactions can be grouped according to different energy transfer regimes that form the basis of the principal experimental techniques. Historically, inelastic electron scattering was developed prior to the availability of continuous energy sources from dedicated storage rings. In fact, under certain circumstances, electronic excitations are equivalent to photon excitations in that they can be described within a common conceptual and theoretical framework.

An electron is an elementary particle with a mass m and, owing to its wave nature, has a de Broglie wave number $k = p/\hbar$, where $\boldsymbol{p} = m\boldsymbol{v}$ is the momentum of the electron, $\boldsymbol{v}$ is its velocity, and $\hbar$ is Plank's constant divided by 2π. The kinetic energy is expressed classically by $E = \frac{1}{2}mv^2$, where $v = |\boldsymbol{v}|$. Electrons have a negative charge e and a nonclassical angular momentum (spin). These properties play a central role in the interactions between electrons and their environment and constitute the basis of a wide range of spectroscopic techniques.

Owing to their unique properties, there are both advantages and disadvantages to using electrons as a probe in analytical applications. Spin-polarized or spin-averaged beam of electrons are readily created, electrons can be accelerated to any energy, and focused on a target at will. After they interact with the target material, electrons can be analyzed according to their intensity, momentum, energy, and spin polarization. In the final state, there are, even in an idealized single-scattering event, two electrons that arbitrarily share the initial energy. These electrons are indistinguishable, which makes the interpretation of the results especially challenging.

Cross-section for inelastic scattering

Electron-atom scattering is the cradle of today's understanding of the quantum mechanics of many solid-state interactions. Electron–solid interactions, however, not only present a wealth of phenomena to aid the development of modern physics, but have also made spectroscopies based on electronic excitations one of the major sources of information on atomic and electronic structure and on the elemental composition of materials. To account for all electronic interactions, a first-principles theory should be developed, though a semiclassical approach often suffices.

The strength of the electronic interaction depends on the electronic energy and the materials, which endows the energy dependence of a type of event with dynamical information about the interaction. If the interaction is weak, the energy $\hbar\omega$ lost by the electron and the associated momentum transfer $\boldsymbol{q}$, involve the creation of a single excitation with an energy $\hbar\omega$ and momentum $\boldsymbol{q}$. In this case, the Born approximation (**Merzbacher, 1961**) is valid, so the initial (i) and final (f) states of the electron are given by plane waves:

$$\psi_i = e^{i\boldsymbol{k}_i\cdot\boldsymbol{r}} \qquad \psi_f = f(\boldsymbol{k}_i)e^{i\boldsymbol{k}_f\cdot\boldsymbol{r}}, \tag{1}$$

where $f(\boldsymbol{k}_i)$ is the scattering amplitude. The interaction between the electron and the environment is described by a Hamiltonian containing the energy of the unperturbed sample, the energy of the electron, and the Coulomb potential $V(\boldsymbol{r})$ between the sample and the electron. During the interaction, energy and momentum are conserved,

$$E_i - E_f = \hbar\omega, \qquad \boldsymbol{k}_f - \boldsymbol{k}_i = \boldsymbol{q}. \tag{2}$$

Using Fermi's golden rule (**Merzbacher, 1961**), the differential scattering cross-section can be expressed as

$$d\sigma = \frac{2\pi}{\hbar}\left|\left\langle \phi_f \psi_f | V | \psi_i \phi_i \right\rangle\right|^2 \delta\left(E_i - E_f\right) d\boldsymbol{k}, \tag{3}$$

where ϕ_i and ϕ_f are the wave functions of the target before and after the scattering, respectively.

When an electron scatters from an atom, the interaction only with the other electrons can be inelastic because no energy is transferred to the nucleus by Coulomb scattering. The most general type of energy transfer in electronic excitations produces a transition from an occupied to an unoccupied state separated by an energy equal to the energy loss of the primary electron. The differential cross-section of such a transition is obtained by integrating Eq. (**3**) to obtain

$$\frac{d^2\sigma}{dEdq} = \frac{8\pi}{q^3 k_i^2}\left(\frac{e^2 m^2}{\hbar^2}\right)^2 \left|\left\langle \phi_f | e^{-i\boldsymbol{q}\cdot\boldsymbol{r}} | \phi_i \right\rangle\right|^2. \tag{4}$$

The cross-section $N(E) \propto d\sigma/dE$ is dominated by processes for which the momentum transfer is small. If $\boldsymbol{q}\cdot\boldsymbol{r} \ll 1$, then $e^{-i\boldsymbol{q}\cdot\boldsymbol{r}} \approx 1 - i\boldsymbol{q}\cdot\boldsymbol{r}$, and the dipole approximation used in optics becomes applicable to inelastic electron scattering:

$$\frac{d^2\sigma}{dEdq} = \frac{8\pi}{q}\left(\frac{e^2}{\hbar^2 v_i}\right)^2 |\phi_f|\boldsymbol{n}\cdot\boldsymbol{r}|\phi_i\rangle|^2, \tag{5}$$

where $v_i = \hbar k_i/m$, $\boldsymbol{q} = q\boldsymbol{n}$, and $\boldsymbol{n}$ is the unit normal vector along $\boldsymbol{q}$.

Interband transitions

The validity of the dipole approximation means that the scattering cross-section can be related to the dielectric properties of the target material. The dielectric response,

$$\varepsilon(\boldsymbol{q},\omega) = \varepsilon_1(\boldsymbol{q},\omega) + i\varepsilon_2(\boldsymbol{q},\omega), \tag{6}$$

depends on the energy transfer $\hbar\omega$ and the momentum transfer $\boldsymbol{q}$ defined in (**2**). Electrons interacting with the target produce a longitudinal perturbation over the long-range dipole fields. These fields attenuate the electron intensity through the absorptive part ε_2 of the dielectric constant. Since the field is screened by $1/\varepsilon$, the electron-loss function can be written as the sum of surface and bulk contributions (**Raether, 1965**; **Froitzheim, 1977**):

$$\begin{aligned} N(E) \quad &\propto -\mathrm{Im}\left[\frac{S}{1+\varepsilon(\boldsymbol{q},\omega)} + \frac{B}{\varepsilon(\boldsymbol{q},\omega)}\right] \\ &\equiv -\mathrm{Im}\left[\frac{1}{\widetilde{\varepsilon}(\boldsymbol{q},\omega)}\right], \end{aligned} \tag{7}$$

where S and B are weighting factors for the surface and bulk, respectively. The cross-section $N(E)$, therefore, contains fundamental information on the dielectric behavior of the bulk and the surface of the sample. A direct link between electron energy losses and the effective dielectric function defined in (**7**) is provided by the Kramers–Kronig relation (**Jackson, 1975**; **Schattschneider and Jouffey, 1995**),

$$\mathrm{Re}\left[\frac{1}{\widetilde{\varepsilon}(\boldsymbol{q},\omega)}\right] = 1 + \frac{2}{\pi}\int_0^\infty \frac{\mathrm{Im}[1/\widetilde{\varepsilon}(\boldsymbol{q},\omega)]}{\omega'^2 - \omega^2}\omega' d\omega', \tag{8}$$

which gives

$$\widetilde{\varepsilon}(\boldsymbol{q},\omega) = \frac{\mathrm{Re}[1/\widetilde{\varepsilon}(\boldsymbol{q},\omega)] - i\mathrm{Im}[1/\widetilde{\varepsilon}(\boldsymbol{q},\omega)]}{[1/\widetilde{\varepsilon}(\boldsymbol{q},\omega)]^2}. \tag{9}$$

The practical advantage of energy-loss measurements over optics lies in the fact that they cover a larger energy range than experiments with photons, which facilitates a more complete evaluation of (**8**). The electron energy-loss function, in fact, depends on the joint density of states (DOS), defined as the convolution of the occupied initial states and the unoccupied final states that are separated by the energy loss and are coupled by the matrix element. The optical function contains the transverse properties of the solid, which may be different from the longitudinal properties accessible to electron energy-loss spectroscopy. The differences between the traverse and the longitudinal responses are negligible for small momentum transfer $\boldsymbol{q}$ (the random phase approximation). For higher values of $\boldsymbol{q}$, multipole transitions are well resolved in electron-induced transitions, but are strictly forbidden in optics.

Inelastic interactions are responsible for the intensity attenuation of electrons within a bulk material. The characteristic quantity for the penetration depth of the electrons is called the mean free path Λ the value of which depends on the available excitations at a particular energy. For the range of energies ~30–100 eV, Λ has values comparable to interatomic distances (**Schnatterly, 1979**). Thus, the experiments contain information mainly on the surface properties (the S-term in **Eq. 7**). In optics, on the other hand, photons penetrate deeply into the target material, so the information is dominated by the bulk DOS (the B-term in **Eq. 7**). Transitions that are characteristic of the surface (e.g., surface states, adsorbates) help to distinguish between bulk and surface excitations.

Plasmon excitations

The cross-section in (**7**) attains peak values for $\varepsilon_1 = 0$ and $\varepsilon_2 = 0$. This condition corresponds to no charge-density fluctuations caused by the incident electrons. A longitudinal plasma wave along the crystal produces long-range Coulomb forces between positive and negative charges and excites collective excitations. These are called plasmons in the case of a quasi-free electron gas. The plasmon energy is obtained from the Fourier modes of the electron density,

$$\rho(\boldsymbol{r}) = \sum_{\boldsymbol{k}} \rho_{\boldsymbol{k}} e^{-i\boldsymbol{k}\cdot\boldsymbol{r}}. \tag{10}$$

The $\rho_{\boldsymbol{k}}$ are amplitudes for harmonic density fluctuations obeying,

$$\frac{d^2\rho_{\boldsymbol{k}}}{dt^2} + \omega_p^2 \rho_{\boldsymbol{k}} = 0, \tag{11}$$

in which ω_p is the Langmuir frequency,

$$\omega_p = \left(\frac{n_e e^2}{\varepsilon_0 m}\right)^{\frac{1}{2}}, \tag{12}$$

n_e is the bulk charge density, ε_0 is the permittivity of free space, and the energy loss due to plasmon creation is $\hbar\omega_p$. Plasmons are quantized excitations, so the energy loss is $n\hbar\omega_p$, where n is a positive integer.

Plasmon energies can be used to extract changes in the electron density that accompany changes of the electronic properties or the volume of a solid. For example, the alloy Al-3 at.% Ag shows a transition from a high-temperature phase, where Al and Ag form a homogeneous solid solution, to a regime ~ 400°C where Ag atoms precipitate as Ag_2Al clusters. The formation of these precipitates can be monitored by observing the plasmon energies of Al across the transition. With Ag atoms homogeneously distributed in the bulk, more volume is available at Al atoms, resulting in a lower effective electron density, thus shifting the plasmon to lower values.

The spectra in **Fig. 1** show that, at 480°C, the plasmon energy is reduced from 15.8 to 15.5 eV signaling a 3.8% volume reduction. At temperatures below 440°C, Ag_2Al precipitates form that are largely decoupled from the aluminum matrix, thus leaving the volume and electron density unaltered from their values in pure Al. Thus, there is no change in the plasmon energy.

Fig. 2 shows high-resolution electron energy-loss spectroscopy (HREELS) measurements of the π and $\sigma + \pi$ plasmons for the indicated monolayers of epitaxial graphene prepared on a Si-terminated 6H-SiC(0001) crystalline wafer by solid state graphitization. The spectra were recorded under identical conditions with the momentum transfer parallel to the surface ($q = 0.1$Å).

The frequencies of the two collective excitation modes shift to higher energies and the peaks broaden as the thickness of the epitaxial layers increases. The changes in the plasmon peaks provide information about how the electronic structure changes with increasing epitaxial thickness. In particular, the 6.3 eV loss peak of the 3-4 monolayers of epitaxial graphene is close to that of graphite. Alternatively, the

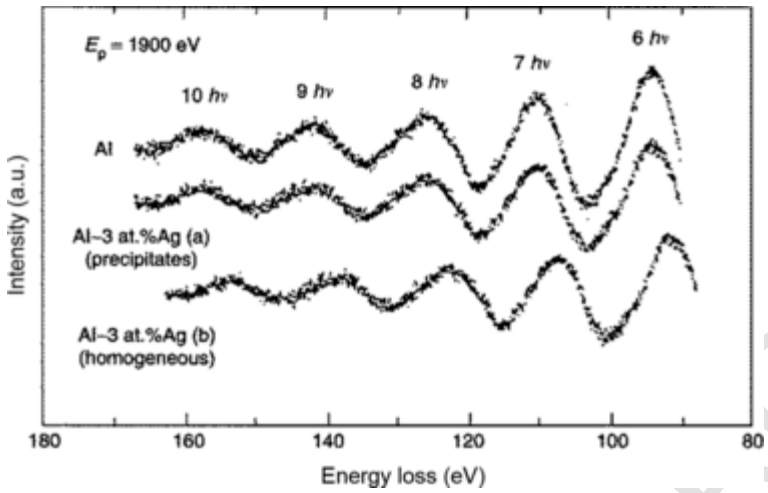

Fig. 1 Energy losses in Pure Al and Al–3 at.% Ag with (A) Ag_2Al precipitates, and (B) Ag atoms homogeneously distributed at 480°C. To accurately determine the plasmon energy, the measurements are extended up to the tenth plasmon loss. Reprinted with permission from Wetli E, Erbudak M, and Schultess T (1994) Segregation and dissolution of Ag-rich clusters at the (100) surface of Al-3 at.%Ag. Physical Review B 49: 14628–14631; © American Physical Society.

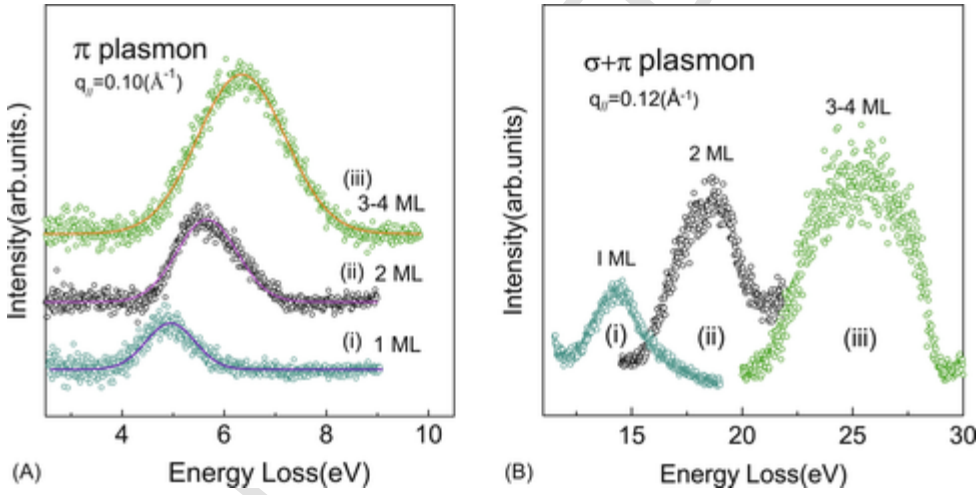

Fig. 2 The (A) π plasmon peak and (B) $\sigma + \pi$ plasmon peak for (i) monolayer, (ii) bilayer, and (iii) 3-4 monolayers of epitaxial graphene. The *solid line* is a Gaussian fit to the data. Reprinted with permission from Lu J, Ping Loh K, Huang H, Chen, W, and Wee ATS (2009) Plasmon dispersion on epitaxial graphene studied using high-resolution electron energy-loss spectroscopy. Physical Review B 80: 113410; © American Physical Society.

intensity of the $\sigma + \pi$ mode becomes weaker with deceasing number of epitaxial layers. The loss peak at 14.5 eV of the $\sigma + \pi$ plasmon peak for single layer epitaxial graphene can be viewed as a limiting case when the out-of-plane mode vanishes, leaving only the in-plane mode.

There are detailed investigations of the dependence of plasmon excitations on the momentum transfer. For increasing values of $\boldsymbol{q}$, the peak in the loss function moves to higher energies until the excitation decays into electron-hole pairs. In semiconductors, electron-hole pairs form a hydrogenic bound state called excitons which, for a material with an indirect band gap, such as Si, have a very long lifetime because the recombination process requires the emission of a phonon to conserve momentum.

Fig. 3 shows the dispersion of π-plasmon energies for epitaxial graphene with different thicknesses. Single layer and bilayer epitaxial graphenes show linear dispersions with q while the 3-4 monolayer structure shows a parabolic dispersion. The linear dispersion of monolayer epitaxial graphene is related to the unique band structure near the K-point of the Brillouin zone. The parabolic dispersion associated with 3-4 layers of epitaxial graphene is similar to the π plasmon dispersion of graphene.

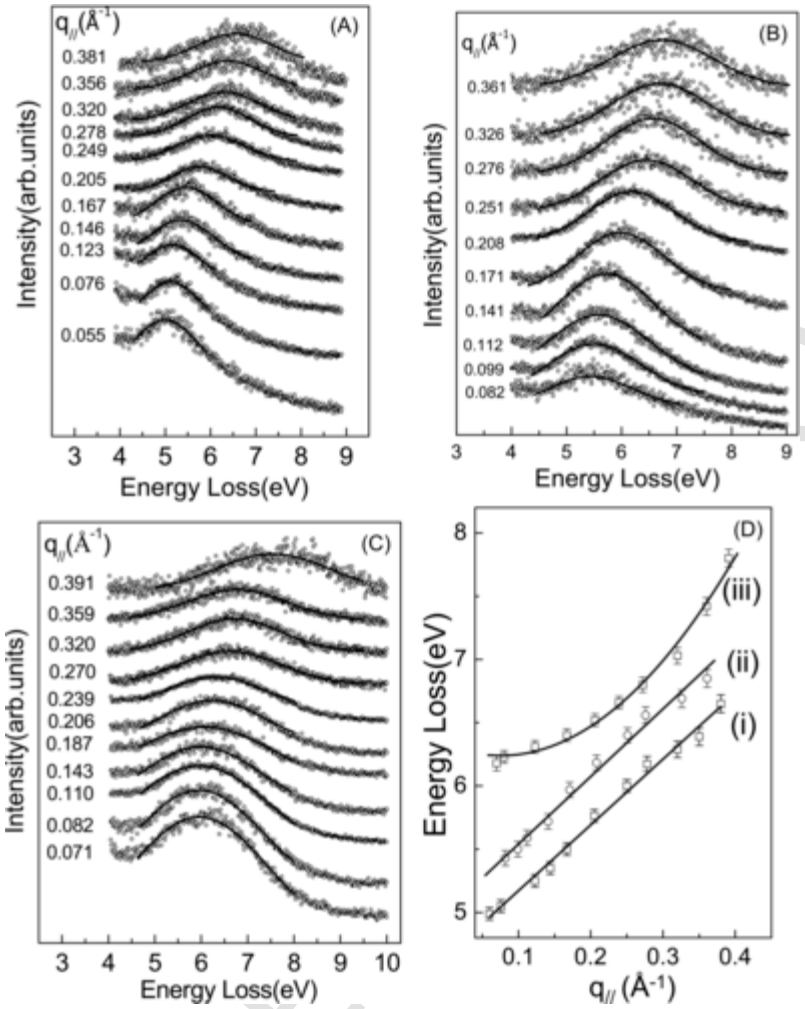

Fig. 3 Measured loss functions associated with the π plasmons of (A) single layer, (B) bilayer, and (C) 3-4 monolayer epitaxial graphene. The data are taken from $q = 0.05$Å to $q = 0.4$Å. The corresponding dispersion curves are shown in (D), for (i) single layer, (ii) bilayer, and (iii) 3-4 layers of epitaxial graphene. Reprinted with permission from Lu J, Ping Loh K, Huang H, Chen, W, and Wee ATS (2009) Plasmon dispersion on epitaxial graphene studied using high-resolution electron energy-loss spectroscopy. Physical Review B 80: 113410; ©American Physical Society.

Vibrations at surfaces

Electrons moving near the surface of a solid can excite localized and collective vibrations. The major experimental achievement in the measurement of these vibrations has been the development of near-monochromatic primary-electron beams and, additionally, the detection of reflected electrons with a resolution of the order of vibrational energies (a few meV). On Si(111), one of the most intensively studied surfaces, the local arrangement of atoms at and near the surface including the stretching of Si-Si bonds, has been obtained from surface phonon measurements and found to be consistent with the dimer-adatom-stacking fault model.

Adsorbates are foreign atoms that are bound to sites with a particular point-group symmetry of the surface structure. If the dipole image charge of the adsorbate has a component normal to the surface, the adsorbate can be excited into vibrational states while the modes with their dipole moment parallel to the surface are screened by a factor $1/(1+\varepsilon)^2$. These selection rules are similar to those governing infrared transitions. One can determine the local symmetry by observing the number of vibrational modes. The local geometry is modeled by a rigid substrate against which the adsorbates vibrate (**Ibach and Mills, 1982**).

Fig. 4 shows some fundamental types of bonding arrangements. In (A), an adsorbate atom is placed at a top position, directly above a surface atom. This site would produce a single low-energy mode. In (B), the same atom is placed in a bridge position, equidistant between two substrate atoms. Energy loss would be observed at an even lower value than (A), corresponding to the normal vibrational component.

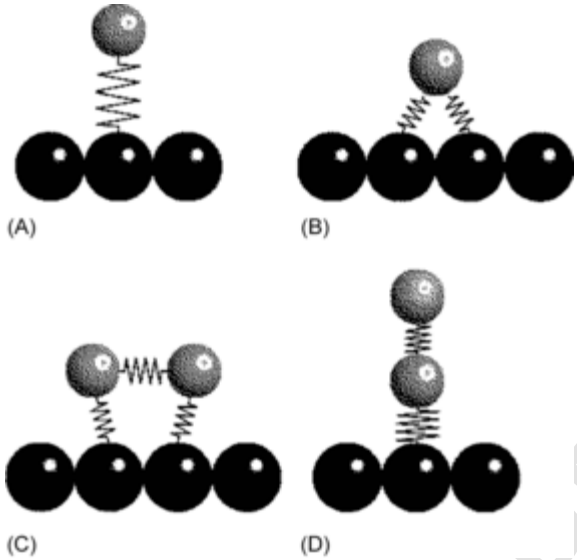

Fig. 4 Schematic description of four typical adsorption states for (A) an atop and (B) a bridge site for single atoms, and (C) a bridge site and (D) and atom site for a diatomic molecule. The springs represent chemical bonds of different strengths.

If the chemical bonding were not symmetrical, then one would observe two peaks at similar energy losses. Generally, a lowering of the adsorption symmetry, such as uneven bonding, increases the number of vibrational modes (**Ibach and Mills, 1982**).

For molecular adsorbates (**Fig. 4**C and D), a high-energy loss would be due to the stretching mode of the atoms in the molecule while a low-energy loss would be due to the vibration of each atom against the substrate or the entire molecule. Hence, for molecular adsorption, one always expects at least two modes. Observation of a single mode is, therefore, evidence for the dissociative adsorption of a molecule. Apart from the number modes, the vibrational energy contains information about the chemical bond. An adsorption site on top of a substrate atom results in a higher force constant compared to an adsorbate at a bridge or hollow site, where the bond strength is shared by several atoms.

Excitation of core electrons

A special case of interband transitions is the excitation of core electrons with a binding energy E_B. The primary electron can transfer any amount of energy $E_L \leq E_i$ to the core electron. By measuring the energy loss of the primary electron, one knows the kinetic energy of the core electron after scattering, that is, how far above E_F the core electron has been excited. The excitation into states at E_F corresponds to zero kinetic energy and, hence, $E_L = E_B$. This is called the absorption edge. It is characteristic of a particular element and its chemical state and can thereby be used as a tool for chemical analysis.

Core states have almost no overlap between neighboring atoms, leading to extremely narrow bandwidths. Therefore, the energy-loss spectrum at and above the absorption edge is indicative of the unoccupied DOS at the site of the excited atom with an orbital angular momentum determined by the symmetry of the final state (**Tinkham, 1964**). If the final states are far above E_F, the modulations in the spectra result from single scattering, which can be used to extract local structural information near the excited atom. This is known as extended energy-loss fine structure (EELFS); the optical analog is extended X-ray absorption fine structure (EXAFS). The information obtained is a radial distribution function with peaks at the distances of nearest neighbors (**Prinz and Koningsberger, 1986**; **Vvedensky, 1992**; **Rehr and Albers, 2000**).

Closer to the absorption edge, the interpretation of the energy-loss near-edge fine structure (ELNES) spectrum requires a multiple scattering treatment, as in the near-edge X-ray-absorption fine structure (NEXAFS) in optics. In this regime, the type of information obtained includes bond angles between the excited atom and its nearest neighbors (**Prinz and Koningsberger, 1986**; **Vvedensky, 1992**; **Rehr and Albers, 2000**).

Nanotubes provide an illustration of such measurements. The chemical and physical properties can be manipulated by incorporating atoms or molecules within the tubes. **Fig. 5** shows a high-resolution electron micrograph of an isolated single-wall nanotube containing C_{82} fullerenes and a schematic representation of the structure. The image reveals single Gd atoms encapsulated in the fullerene cages.

Fig. 6 displays spatially resolved ELNES spectra of the C *K*-edge (1*s* initial state) and the Gd *N*-edge (4d-initial state). Thus, it is possible to detect and identify single Gd atoms encaged in a complex C environment. Core-electron binding energies may show a chemical shift because the electronic charge density is redistributed in chemical bonding, thereby shifting the binding energy. The core electron binding energy of Gd shows a downward shift compared to the neutral Gd metal, which suggests a charge transfer from Gd to a C atom.

Detecting the local environment of Si in a graphene lattice has elements of local symmetry, as for lattice vibrations, and on the local bonding environment. Because of multiple scattering, and therefore, multi-atom correlations, ELNES is sensitive to both of these quantities. This goes far beyond the average local radial distribution function, a single-scattering quantity, obtained in EELFS. Si is one of the most common impurities in graphene grown by chemical vapor deposition or thermal decomposition. Thus, a better understanding of this impurity is desirable for the integration of graphene-based devices onto a silicon platform.

Fig. 7 shows the local environment of a threefold- and a fourfold-bonded Si in a graphene lattice, the corresponding ELNES measurements, and relaxed density-functional calculations. The *L*-edge (2*p* initial state) reflects the excitation to unoccupied 3*d* states. The observed differences in the ELNES of the two coordinations are a direct indication of the occupancy of the 3*d* states due to the different coordinations. In particular, the peak at 105 eV and the shoulder at ~101 eV for the threefold coordinated site were reproduced by the calculations. Moreover, the absence of the peak at 105 eV but the presence of weaker peaks at ~102 eV and 107 eV were also confirmed by the calculations.

The relaxed structures of the threefold and fourfold coordinated Si impurities in graphene are shown in **Fig. 7**A. The calculations used a 200-atom graphene supercell using the Vienna *Ab-Initio* Software Package (VASP) (**Hafner, 2008**). For the threefold coordinated site, the silicon atom is displaced outward from the graphene surface. The fourfold Si impurity site, however, stays largely in the plane of the graphene. The threefold calculations are consistent with previous calculations while the fourfold calculations agree with conclusions drawn from experimental data.

$(e^-, 2e^-)$ Scattering

A general, yet simple, case of electron–atom or electron–solid interactions is considered in this section. Denoting the energy and momentum of the primary electron by superscript 1 and those of the target by superscript 2, the initial values (subscript *i*) are

$$\begin{aligned} \text{primary electron}: &\quad E_i^{(1)}, \quad \boldsymbol{k}_i^{(1)} \\ \text{target}: &\quad E_i^{(2)}, \quad \boldsymbol{k}_i^{(2)}. \end{aligned} \tag{13}$$

The corresponding final states (subscript *f*) are

$$\begin{aligned} \text{primary electron}: &\quad E_f^{(1)}, \quad \boldsymbol{k}_f^{(1)} \\ \text{target}: &\quad E_f^{(2)}, \quad \boldsymbol{k}_f^{(2)}. \end{aligned} \tag{14}$$

In the limit of large energy and momentum transfer, $E_f^{(1)}$ and $E_f^{(2)}$ are well above the band structure regime, so the unoccupied DOS is parabolic and does not impose additional structure upon the measurement. This interaction regime is the basis of $(e^-, 2e^-)$ spectroscopy for solids (**McCarthy and Weigold, 1991**; **Artamonov et al., 1997**). For atomic or molecular targets $(e^-, 2e^-)$, spectroscopy provides information about the wave function density in momentum space by measuring the momentum distribution of the bound electron as a function of the momentum transfer. For crystalline targets, both the momentum density and the energy dispersion of valence electrons can be determined. Since the momentum of any ejected electron can be measured, the results are not confined to the first Brillouin zone.

In a binary collision between a high-energy electron and a band electron, the conservation of energy and of momentum requires that

$$\begin{aligned} E_i^{(1)} &= E_f^{(1)} + E_f^{(2)} + E_i^{(2)}, \\ \boldsymbol{k}_i^{(1)} &= \boldsymbol{k}_f^{(1)} + \boldsymbol{k}_f^{(2)} + \boldsymbol{k}_i^{(2)}. \end{aligned} \tag{15}$$

There is, however, a continuous spectrum of single- and multiple-scattering events leads to $E_f^{(1)} + E_f^{(2)}$. To single out the event for which both conservation equations hold, the particles must be recorded in coincidence.

Fig. 8A shows the geometry of primary electrons impinging on a solid sample. A binary collision event is depicted in which a target electron acquires energy and is ejected from the back of the sample together with the primary electron. For simplicity, the scattering event is shown with coplanar initial and final wave vectors. In general, the 2π azimuthal distribution relative to the primary-electron incidence is measured to access the details of the initial state (**Fig. 8B**). Energy conservation requires the binary collision event to take place as close to the surface as possible, so inelastic interactions after the principal collision are not considered. Consequently, the spectroscopic results are characteristic of the near surface region of the target material.

Fig. 9 shows an energy-band dispersion in graphite along the indicated directions in the Brillouin zone. Graphite has four populated bands, three of σ-type and one of π-type. No intensity is expected in the Γ–*M* and Γ–*K* directions from the π-band because the band is derived from C 2*p* orbitals will have a node at $q_z = 0$. Along the Γ–*M* direction, the lowest σ band, σ_1 disperses upward and crosses the first Brillouin zone boundary at $q = 0.8$ a.u. In the second Brillouin zone, the second σ band, σ_2, is populated and the small splitting between σ_1 and σ_2 is not resolved. The σ_2 band continues to a maximum at $q = 1.6$ a.u., where the occupation of this band decreases and no intensity is observed above this maximum.

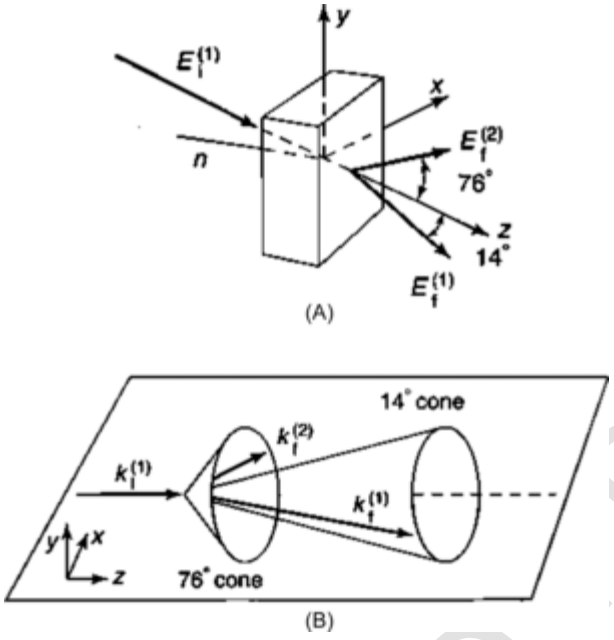

Fig. 8 Schematic illustration of energy conservation in an (e^-, $2e^-$) experiment. (A) Geometry of primary electrons impinging on a sample, and (B) the 2π azimuthal distribution relative to the primary-electron incidence. Adapted with permission from Cai YQ, Vos, M, Stoner, P, Kheifets AS, MacCarthy IE, et al. (1995) Direct imaging of the valence electronic structure of solids by (e, $2e$) spectroscopy. Solid State Communications 95: 25–29.

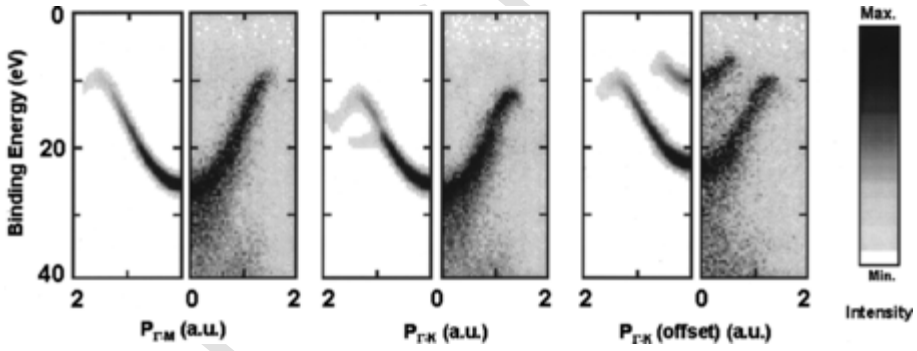

Fig. 9 Measured intensity (right half of each panel) as a function of binding energy and momentum of graphite along Γ-M (left), Γ–K (center), and offset Γ–K (right). Shown with these measurements are the results of density functional calculations (left half of each panel). Adapted with permission from Vos C, Fang Z, Canney S, Kheifets A, McCarthy IE, and Weigold E (1997) Energy-momentum density of graphite by (e, $2e$) spectroscopy. Physical Review B 56: 963–966; ©American Physical Society.

Along the Γ–K direction, the σ_1 band reaches the Brillouin zone boundary at a somewhat larger momentum (q = 0.9 a.u.), where the population changes from the σ_1 band to the third σ_3 band. Continuing to the third Brillouin zone, the σ_3 band reaches a maximum at M for momentum $q \approx 1.3$ a.u. The momentum density decreases beyond this point and the band turns over in the experimental density plot. Finally, with a nonzero offset $q_z = 0.41$ a.u., we expect the π band to be occupied. Two parabolas are observed, one for the π band and one for the σ band. The offset excludes zero momentum, so the measured bottom of the σ band has moved up in energy accordingly.

All of the foregoing features are reproduced by density functional calculations, using a linear muffin-tin orbital (LMTO) model, convoluted with a 2 eV energy broadening and 1 eV momentum broadening, which are shown in **Fig. 8**.

Summary and outlook

Electron energy-loss spectroscopy is based on the measurement of electrons that have lost energy to a target specimen due to inelastic collisions. Several examples of such measurements have been provided: interband transitions, plasmon excitations, vibrations at surfaces, core-level spectroscopy, and (e^-, $2e^-$) scattering. When combined with transmission electron microscopy (TEM), electron energy-loss spectroscopy is capable of a spatial resolution down to the atomic level (**Spence, 2006**; **Egerton, 2009, 2011**; **Krivanek et al., 2014**). This is seen in **Figs. 5–7**. Another advance is the combined use of scanning tunnelling microscopy and TEM (**Suenaga and Koshino, 2010**) to differentiate between different bonding environments near, for example, a graphene edge.

Theoretical and computational studies supplement electron energy-loss experiments. These take the form of selection rules for atomic, molecular, and solid-state systems (**Tinkham, 1964**), a multiple scattering analysis of the dominant paths (**Vvedensky and Pendry, 1985**), or a full density functional calculation (**Hafner, 2008**). **Fig. 7** provides an example of the latter type of calculation. By comparing fully relaxed structures with ELNES measurements, the symmetry of the site should be determined along with any relaxation out of the graphene plane. Thus, density functional calculations expand the spatial range of ELNES measurements to below atomic length scales.

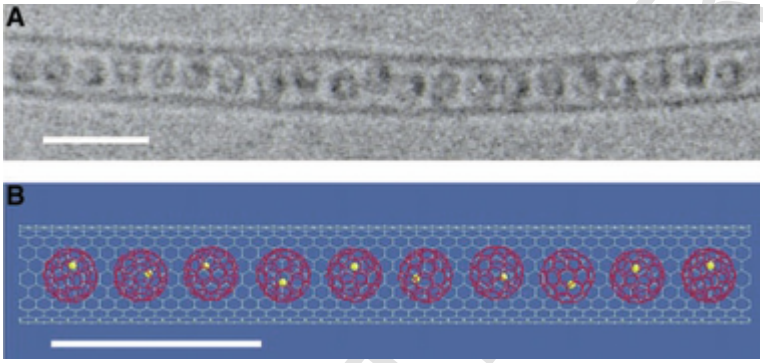

Fig. 5 (A) Electron micrograph of an isolated nanotube incorporated with a chain of Gd-metallofullerenes, and (B) a schematic representation of the structure. *Horizontal bars* represent a length of 3 nm. Reprinted with permission from Suenaga K, Tencé M, Mory C, Colliex C, Kato H, et al. (2000) Element-selective single atom imaging. Science 290: 2280–2282; ©AAAS.

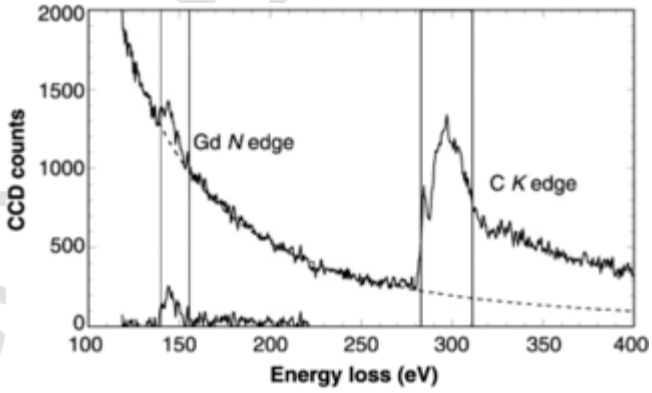

Fig. 6 Electron energy-loss spectra near the Gd *N*-edge and C *K*-edge obtained from an isolated nanotube incorporated with a chain of Gd-metallofullerenes. Reprinted with permission from Suenaga K, Tencé M, Mory C, Colliex C, Kato H, et al. (2000) Element-selective single atom imaging. Science 290: 2280–2282; ©AAAS.

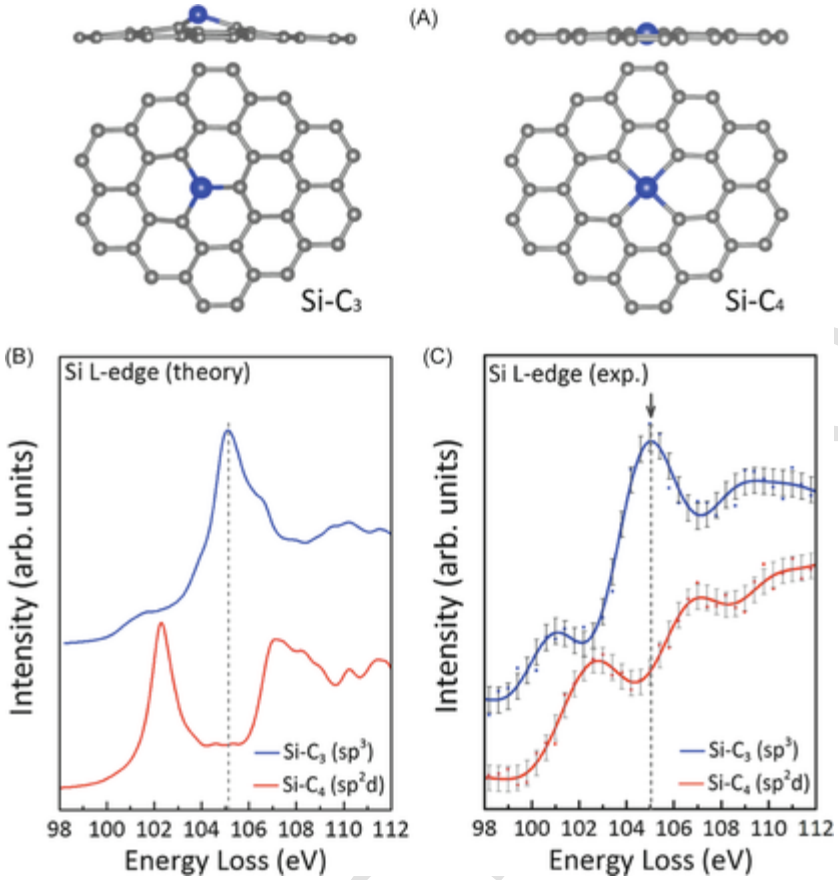

Fig. 7 (A) Three-dimensional relaxed structures for the three-fold and four-fold Si defect structures in graphene. The Si atom is indicated in *blue* and the C atoms in graphene *gray*. (B) Calculated Si *L*-edge spectra for the three-fold (top) and four-fold (bottom) coordinated Si defect structures in graphene. (C) Measured ELNES for the three-fold (top) and four-fold (bottom) coordinated Si defect structures. Adapted from Zhou W, Kapetanakis MD, Prange MP, Pantelides ST, Pennycook SJ and Idrobo J-C (2012) Direct determination of chemical bonding of individual impurities in graphene. *Physical Review Letters* 109: 206803; ©American Physical Society.

References

Artamonov, O.M., Samarin, S.N., and Kirschner, J. (1997) (*e*, 2*e*) Electron spectroscopy of surfaces. *Applied Physics A* 65: 535–542.

Egerton, R.F. (2009) Electron energy-loss spectroscopy in the tem. *Reports on Progress in Physics* 72: 016502.

Egerton, R.F. (2011) Electron Energy-Loss Spectroscopy in the Electron Microscope. Springer, New York.

Froitzheim, H. (1977) Electron energy loss spectroscopy. In: Ibach, H. (ed.), *Electron Spectroscopy for Surface Analysis*. In: Topics in Current Physics, 4. pp. 205–250, Springer, Berlin.

Hafner, J. (2008) Ab-initio simulations of materials using VASP: Density-functional theory and beyond. *Journal of Computational Chemistry* 29: 2044–2078.

Ibach, H. and Mills, D.L. (1982) Electron Energy Loss Spectroscopy and Surface Vibrations. Academic Press, New York.

Jackson, J.D. (1975) Classical Electrodynamics. second ed. Wiley, New York.

Krivanek, O.L., Lovejoy, T.C., Dellby, N., Aoki, T., Carpenter, R.W., Rez, P., Soignard, E., Zhu, J., Batson, P.E., Lagos, M.J., Egerton, R.F., and Crozier, P.A. (2014) Vibrational spectroscopy in the electron microscope. *Nature* 514: 209–212.

McCarthy, I.E. and Weigold, E. (1991) Electron momentum spectroscopy of atoms and molecules. *Reports of Progress in Physics* 54: 789–879.

Merzbacher, E. (1961) Quantum Mechanics. third ed. Wiley, New York.

Prinz, R. and Koningsberger, K. (1986) X-Ray Absorption: Principles, Applications and Techniques of EXAFS, SEXAFS, and XANES. Wiley, New York.

Raether, H. (1965) Solid state excitations by electrons. In: Höhler, G. (ed.), *Springer Tracts in Modern Physics*, 38. pp. 85–157, Springer, Berlin.

Rehr, J.J. and Albers, R.C. (2000) Theoretical approaches to x-ray absorption fine structure. *Reviews of Modern Physics* 72: 621–654.

Schattschneider, P. and Jouffey, B. (1995) Plasmons and related excitations. In: Reimer, L. (ed.), *Energy-Filtering Transmission Electron Microscopy*. In: Springer Series in Optical Sciences, 71. pp. 151–224, Springer-Berlin.

Schnatterly, S.E. (1979) Inelastic electron scattering spectroscopy. In: Ehrenreich, H., Seitz, F., Turnbull, D. (eds.), *Solid State Physics*, 34. Academic Press, New York.

Spence, J.C.H. (2006) Absorption spectroscopy with sub-angstrom beams: ELS in STEM. *Reports on Progress in Physics* 69: 725–758.

Suenaga, K. and Koshino, M. (2010) Atom-by-atom spectroscopy at graphene edge. *Nature* 468: 1088–1090.
Tinkham, M. (1964) Group Theory and Quantum Mechanics. MacGraw-Hill, New York.
Vvedensky, D.D. (1992) Theory of x-ray absorption fine structure. In: Fuggle, J.C., Inglesfield, J.E. (eds.), *Unoccupied Electronic States*. In: Topics in Applied Physics, 69. pp. 139–201, Springer, Berlin.
Vvedensky, D.D. and Pendry, J.B. (1985) Comment on "experimental study of multiple scattering in x-ray-absorption near-edge structure". *Physical Review Letters* 54: 2725.